

Article

Experimental Study on the Mechanical Behavior and Failure Characteristics of Layered Coal at Medium Strain Rates

Kun Zhong^{1,2}, Wusheng Zhao^{1,*}, Changkun Qin^{1,2} and Weizhong Chen¹

¹ State Key Laboratory of Geomechanics and Geotechnical Engineering, Institute of Rock and Soil Mechanics, Chinese Academy of Sciences, Wuhan 430071, China; zhongkun17@mails.ucas.edu.cn (K.Z.); ckqin_whrsm@163.com (C.Q.); wzchen@whrsm.ac.cn (W.C.)

² University of Chinese Academy of Sciences, Beijing 100049, China

* Correspondence: wszhao@whrsm.ac.cn; Tel.: +86-027-8719-8211

Abstract: The study of the mechanical properties and failure behaviors for coal with different bedding structures at various medium strain rates is of great importance for revealing the mechanism of rock burst. In our study, we systematically analyze the uniaxial compressive strength (UCS), acoustic emission (AE) characteristics, failure pattern, and risk of rock burst on coal specimens with two bedding orientations under ranged in strain rates from 10^{-4} s^{-1} to 10^{-2} s^{-1} . The results reflect that and the bedding direction and the strain rates significantly affect the UCS and failure modes of coal specimens. The UCS of coal specimens with loading directions perpendicular to bedding planes (horizontal bedding) increases logarithmically with increasing strain rate while the UCS increases first and then decreases of coal specimens with loading directions parallel to bedding planes (vertical bedding). The AE cumulative energy of the specimens with horizontal bedding is an order of magnitude higher than that of specimens with vertical bedding. However, it is independent of the strain rates. The energy release rates of these two types of bedded coal specimens increase in a power function as the strain rate increases. The coal specimens with horizontal bedding show violent failure followed by the ejection of fragments, indicating a high risk of rock burst. On the other hand, the coal specimens with vertical bedding exhibit a tensile splitting failure with a low risk of rock burst. Strain localization is a precursor of coal failure, and the concentration area of local principal strain is highly consistent with the initial damage area, and the area where the principal strain gradient is significantly increased corresponds to the fracture initiation area.

Keywords: strain rates; bedding planes; energy density; failure; deformation field; rock burst



Citation: Zhong, K.; Zhao, W.; Qin, C.; Chen, W. Experimental Study on the Mechanical Behavior and Failure Characteristics of Layered Coal at Medium Strain Rates. *Energies* **2021**, *14*, 6616. <https://doi.org/10.3390/en14206616>

Academic Editors: Jens Birkholzer, Yulong Chen, Junwen Zhang, Jianhang Chen and Xuejie Deng

Received: 30 August 2021

Accepted: 10 October 2021

Published: 13 October 2021

Publisher's Note: MDPI stays neutral with regard to jurisdictional claims in published maps and institutional affiliations.



Copyright: © 2021 by the authors. Licensee MDPI, Basel, Switzerland. This article is an open access article distributed under the terms and conditions of the Creative Commons Attribution (CC BY) license (<https://creativecommons.org/licenses/by/4.0/>).

1. Introduction

Deep mining of coal seams occurs in a complex working environment that features high stress, high temperature, and large depth [1]. Deep coal extraction is facing the increasing rock burst disasters of coal mines. Many typical rock burst accidents have occurred in Poland [2,3], the United States [4], Australia [5], Russia [6], and many other countries. Coal mining and excavation activities disturb the original in-situ three-dimensional stress state, resulting in mining-induced dynamic stress [7]. Dynamic loads in coal mines are primarily caused by strata suddenly rupture, fault reactivation, coal pillar instability, coal bumps, and gas outbursts [8–11], which is sometimes called mine earthquake [12]. The energy generated by microseismic events may lead to an increase in the stress of coal [13,14]. The mechanical properties in coal and other rock-like materials change with the strain rates, which has been widely recognized that correlations exist between mechanical parameters and strain rates [15–17]. Therefore, the study of the mechanical behaviors and failure characteristics of coal under mining-induced loading with different strain rates is particularly important.

There is no clear definition of dynamic and static loading rate in coal mines, because it is different from the traditional definition of rock mechanics and closely related to the

stress environment of coal and rock mass [18–20]. He et al. [12] obtained the close relation between strain rates and stress wave excited by dynamic loads through an in-situ test in a coal mine. Compared to explosions, air blasts, dynamic compaction, and piling, the maximum strain rates induced by dynamic loading of coal mines range from 10^{-3} to 10^{-1} s^{-1} , which are considered to be medium strain rates [21]. However, most dynamic tests of coal specimens using high strain rates rely on SHPB [22–25], which is inconsistent with the actual dynamic loading rates in coal mines. Therefore, it is necessary to carry out dynamic experimental studies at medium strain rates for understanding the mechanism of mine earthquakes, rock bursts, and gas outbursts.

Huang et al. [26] concluded that loading rates have a significant effect on the mechanical properties of coal, and even soft coal exhibits a significantly high strength at a certain dynamic loading rate, showing characteristics similar to hard coal. Compared to granite, diorite, quartzite, and other hard rocks, coal is considered a “soft rock”. Its peak stress increases significantly as strain rate increases, and the ratio of stress increment is considerably larger than that in brittle and hard rocks [27]. Many scholars have studied the effect of strain rate on deformation, mechanical properties and failure characteristics, and acoustic emission (AE) parameters of rock samples. For instance, Zhao et al. [28] acquired an empirical formula to describe the effect of strain rate on the peak strength through the uniaxial loading experiments for coal specimens under various medium strain rates. Liang et al. [29] analyzed the effects of strain rates on the failure process, fracture properties, and micro fracture mechanism of rocks under a series of medium and low strain rates of 10^{-5} – 10^{-1} s^{-1} . Cao et al. [7] studied the AE parameters, damage evolution, and mechanical properties of rock specimens under different dynamic loading rates in a coal mine in Xinjiang; they demonstrated that the loading rates significantly influence the AE events, hits and counts decrease in power functions while the AE energy increases. Similarly, Liu et al. [30] explored the effect of strain rate on rock fracture characteristics, AE features, and rupture evolution.

The essence of rock failure is the result of the initiation of new cracks and the expansion and combination of primary cracks under external loading. The study of deformation and fracture is significant to understand the damage and failure processes of rock materials [31]. Li et al. [32] used the modified split Hopkinson pressure bar (SHPB) to investigate the failure mechanisms of rocks with combined flaws under static and dynamic loads, and the Digital image correlation (DIC) method to record the fracture process in real-time. Song et al. [33] studied the fracture and damage distribution characteristics of sandstones by a uniaxial compression test. Dong et al. [34] used the DIC technique to analyze the fracture process at the interface of rock-concrete composite beams with different pre-existing cracks by three-point bending tests.

In addition to the effect of strain rate, the impact of bedding orientation in coal should also be paid attention to [35]. Natural coal, as a typical heterogeneous material, has abundant bedding planes, complex joints, and cleat structures, resulting in heterogeneous mechanical properties and deformation characteristics [36,37]. Liu et al. [38] conducted uniaxial compression tests of strain rates ranged from 10^{-5} to 10^{-2} s^{-1} , and found the differences in the uniaxial compressive strengths and failure modes for coal specimens with the loading direction perpendicular to the bedding (horizontal bedding) and those parallel to bedding (vertical bedding). Tan. et al. [22] studied the dynamic properties of coal containing different bedding planes and under different dynamic loads, their results showed that the mechanical properties change because of the existence of bedding planes, and that the angle between the bedding planes and the loading direction has a significant impact on the weakening effect in strength. Li et al. [25] used a vertical SHPB to perform a dynamic compression test on raw coal specimens that were cored in three directions. They concluded that the peak stress is the largest when the loading direction is perpendicular to the bedding plane, and the smallest when the dip angle is 45° . Bedding properties of coal are important in controlling the anisotropy of mechanical and failure properties. However, only limited studies have considered the anisotropy of coal.

A large number of scholars have studied the mechanical behaviors and failure modes of coal under mining-induced dynamic loading conditions. However, few of these studies have covered the full range of dynamic strain rates and considered the bedding direction effects at the same time. In our study, we conducted uniaxial compression tests on coal specimens with loading directions both perpendicular to and parallel to bedding planes. Subsequently, we revealed the mechanical properties, failure patterns, and risk of bursts from these coal specimens under mining-induced dynamic strain rates ranged from 10^{-4} to 10^{-2} s^{-1} . Furthermore, we used the DIC technique to analyze the pre-failure global strain field of the specimens and discuss the relationship between the principal strain gradient and the specimen failure.

2. Experimental Methods

2.1. Specimens Preparation

Raw coal blocks were taken from the Man Jialiang Coal Mine, Ordos City, Inner Mongolia Autonomous Region, China. In this study, we chose raw coal samples to better represent field conditions. Inevitably, raw coal samples often contain natural fractures or cleats, which just reflects the nature of coal. To improve the accuracy of the experiments, our coal samples were taken from the same raw coal block with similar fractures and degrees of weathering. The coal specimens were cored perpendicular to the bedding direction (Figure 1a), and parallel to the bedding direction (Figure 1b). In addition, these specimens were cut and polished into a standard dimension with a cylinder size of $50 \text{ mm} \times 100 \text{ mm}$ (diameter \times height), as specified by the International Society for Rock Mechanics (ISRM).

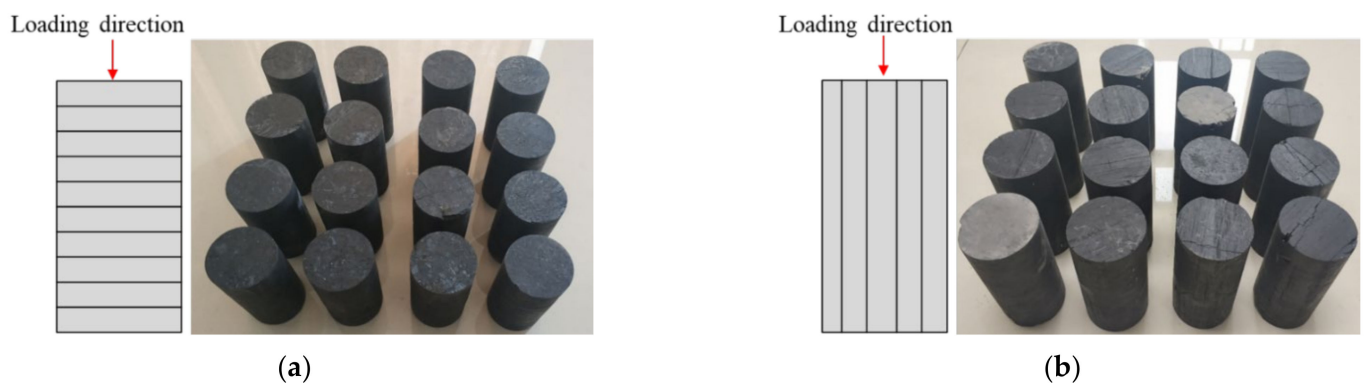


Figure 1. Coal specimens: (a) horizontal bedding; (b) vertical bedding.

2.2. Loading Scheme and Monitoring Techniques

Figure 2 shows the experimental apparatus, consisting of an RMT-201 loading system, an AE monitoring system, and a DIC observation system. These components are synchronized when the specimen is loaded.

The strain rate range statistics of mine seismic induced dynamic loads are obtained through an in-situ test [12]. Therefore, a displacement control model was used in the RMT-201 loading system during uniaxial compression experiments, and the loading rates were 10^{-4} , 5×10^{-4} , 10^{-3} , 5×10^{-3} , and 10^{-2} s^{-1} , well-covering strain rates for coal mines. Table 1 lists the experimental schemes and specific parameters for the experiments. To avoid the randomness of the experimental results, these tests were carried out under the same testing condition, and the average value was taken as the final experimental results.

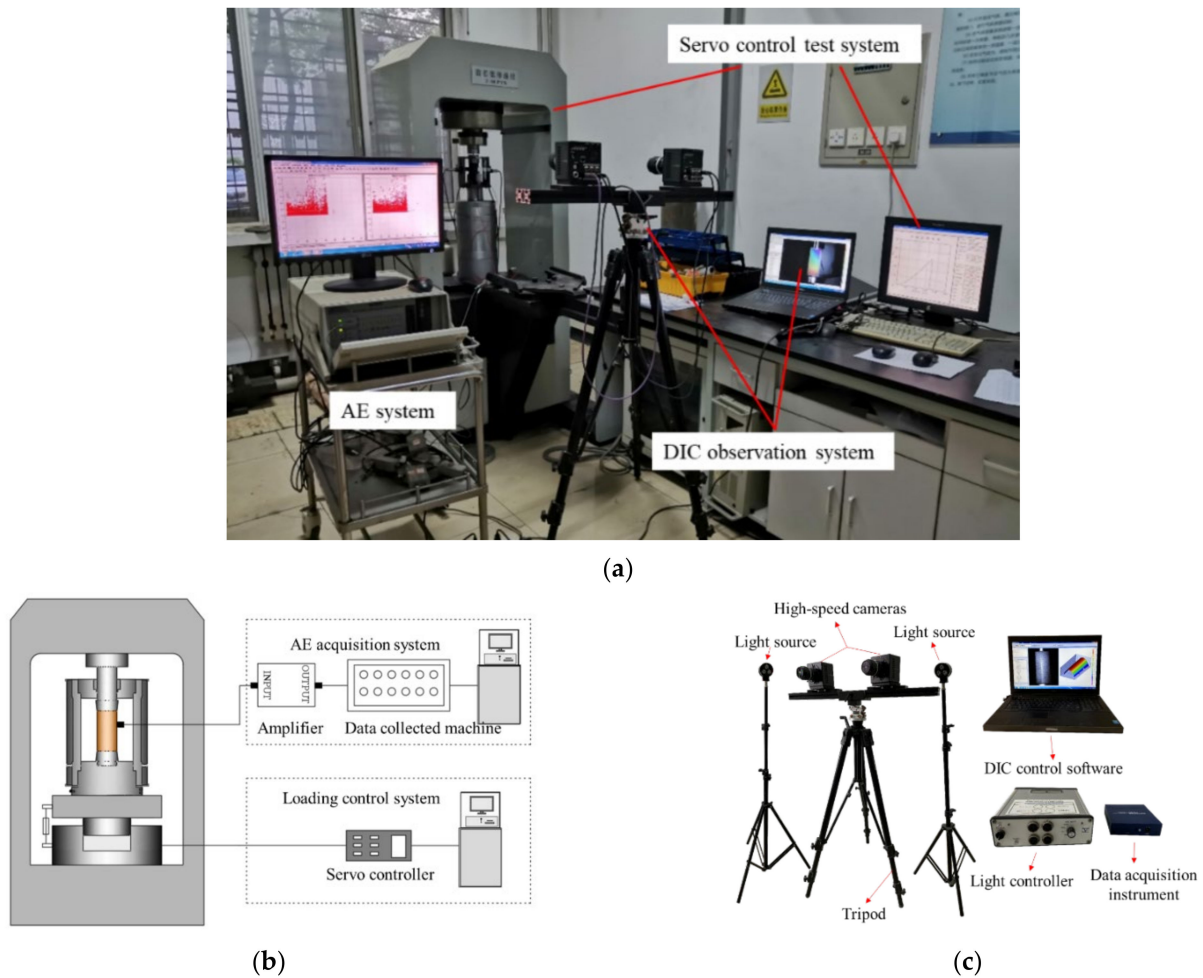


Figure 2. The experimental apparatus: (a) full view; (b) AE system and loading cell; (c) 3D-DIC observation system.

Table 1. Experiment schemes.

Bedding Direction.	Specimen Number	Strain Rate/s ⁻¹
Perpendicular to loading direction (horizontal bedding)	H1	1×10^{-4}
	H2	5×10^{-4}
	H3	1×10^{-3}
	H4	5×10^{-3}
	H5	1×10^{-2}
Parallel to loading direction (vertical bedding)	P1	1×10^{-4}
	P2	5×10^{-4}
	P3	1×10^{-3}
	P4	5×10^{-3}
	P5	1×10^{-2}

The MISTRAS series PCI-2 system produced by the American Physical Acoustics Company was used as the AE monitoring system. This system has the advantages of high monitoring accuracy, low noise, and low power consumption, and can simultaneously record extract characteristic parameters such as event number, event count, amplitude, energy, and frequency.

Figure 2c shows the DIC observation system, including cameras, light sources, a data acquisition instrument, and a DIC control software. Two GT3400 high-speed cameras were used in this study (the resolution is 3384×2074 , lens focal length 80 mm) to continuously take the images of specimen surfaces and record the data acquisition instrument. And start

trigger mode was used to take photos in the dynamic loading stage. The DIC software can collect full-field deformation and strain for localized deformation analysis under various loading conditions. Speckles need to be sprayed on the surface of the specimens for the full-field strain measurements using the DIC technique, as shown in Figure 3. Once a specimen is loaded, the speckles on the surface will move with the deformation of the specimen, so they can be regarded as markers on the surface of the specimen and used to evaluate the displacement field. By using two digital images before and after deformation, the displacement and strain fields of the specimen surface are obtained by image matching technology and registration algorithm.



Figure 3. Some speckled specimens.

3. Test Results and Discussion

3.1. Deformation Evolution and Failure Mode

We take typical (Specimens numbers H4 and P4, shown in Table 1) specimens with different bedding directions as examples to analyze the crack propagation process. H4 represents the #4 specimen with horizontal bedding, and P4 represents the #4 specimen with vertical bedding. As shown in Figure 4, the surface of specimen H4 with horizontal bedding was first partially peeled off, and then the peeling range was further expanded to form a through-going shear plane. Figure 5 shows the failure evolution process of specimens P4 with vertical bedding. Several vertical cracks were generated first on the specimen surface, and then the main crack was widened, resulting in the ultimate vertical splitting.

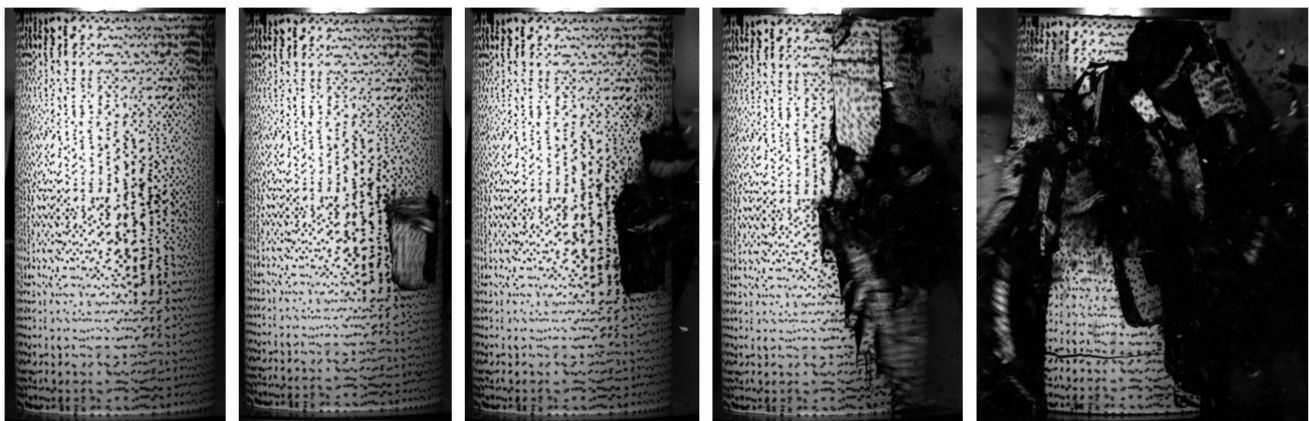


Figure 4. The failure process of specimen H4.

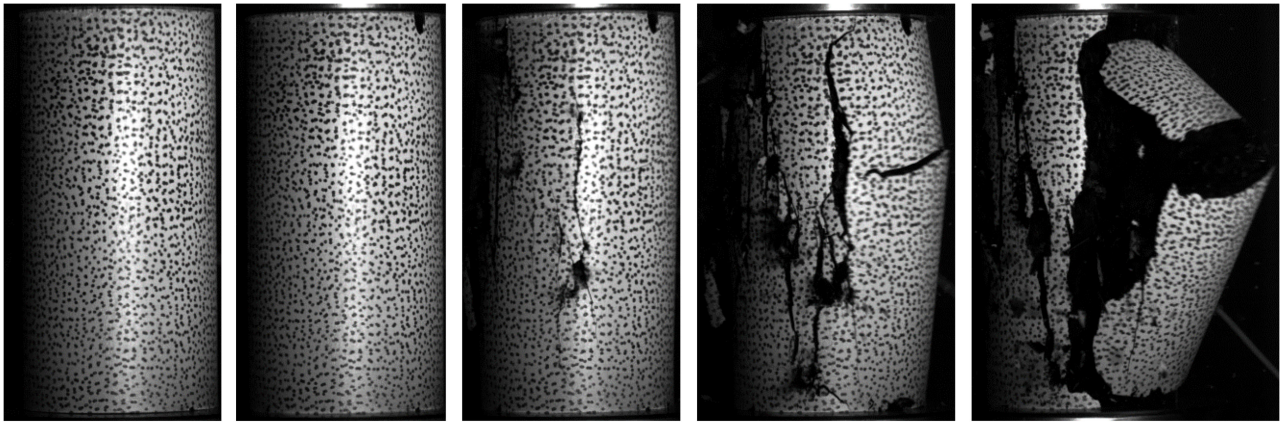


Figure 5. The failure process of specimen P4.

The crack growth and failure process of specimens with different bedding planes during the entire loading process were captured by high-speed cameras. The specimens with horizontal bedding were unstable and burst into small pieces, so the photos for these specimens were taken by a high-speed camera before bursting. The fracture surfaces of the coal specimens with vertical bedding were visible after the failure, so the failure patterns can be captured with a normal-speed camera. Table 2 shows the failure modes of coal specimens with two different bedding directions under different strain rates.

Table 2. Failure modes of coal specimens.

Strain Rate/Bedding	$1 \times 10^{-4} \text{ s}^{-1}$	$5 \times 10^{-4} \text{ s}^{-1}$	$1 \times 10^{-3} \text{ s}^{-1}$	$5 \times 10^{-3} \text{ s}^{-1}$	$1 \times 10^{-2} \text{ s}^{-1}$
Horizontal bedding					
Vertical bedding					

The coal specimens with horizontal bedding generally exhibit burst failure behavior, accompanied by the ejection of fragments of different sizes. With the increase of strain rate, the bursting becomes more violent. The overall failure is a tensile-shear failure mode. The fracture surface is not affected by weak planes, and the strength of these specimens

is similar to that of intact specimens [39]. The failure mode of the coal specimens with vertical bedding is a tensile splitting failure, and many defects and cracks are created. Table 2 shows that the failure mode of coal specimens does not change at different strain rates. Coal, a typical soft rock, does not exhibit a strong strain rate-dependent failure mode, which is different from other rocks [31], indicating that the rate-dependence of failure mode may be related to rock types.

Local damage occurs before the complete failure in coal, and strain localization is a precursor to the failure of coal specimens. Therefore, studying the evolution of the global deformation field is of significance to understanding failure characteristics and early warning. For the sake of space, in this paper we will just show the detailed results of coal specimens H4 with a strain rate of $5 \times 10^{-3} \text{ s}^{-1}$, because this strain rate is the closest to the strain rate range of the coal mine. We will discuss in detail the relationship between strain evolution and crack initiation and propagation.

Figure 6 shows the stress-strain curve of specimen H4 and five images at key stages. The five key stages represent the different loading times, corresponding to the load that is 13.9 MPa, 23.7 MPa, 34.1 MPa, 34.2 MPa, and 32.6 MPa. The global principal strain fields (the maximum tensile strain) at these five points are shown in Figure 7. Since it is impossible to calculate part of the area at the edge of the specimen, the actual calculated size is $40 \text{ mm} \times 90 \text{ mm}$, which is smaller than the initial specimen size. During the initial stage of loading, the specimen was deformed uniformly, as shown in Figure 7a. Strains in the compaction stage and the initial linear elastic stage are both less than 0.4%. Figure 7b corresponds to the key point “b”, at this point, a small area of local strain concentration occurred in the specimen. Figure 7c corresponds to the pre-peak stage, in which the area of local strain concentration and strain magnitude on the right side of the specimen were further expanded. At the peak point “d”, local spalling started to take place on the specimen surface, and the strain concentration area did not further expand. The strain magnitude, however, significantly increased, and the strain gradient in this area was larger than that in the rest of the areas. At the post-peak stage, the peeling area on the specimen surface at the “e” point was further expanded until the specimen reached the complete burst failure.

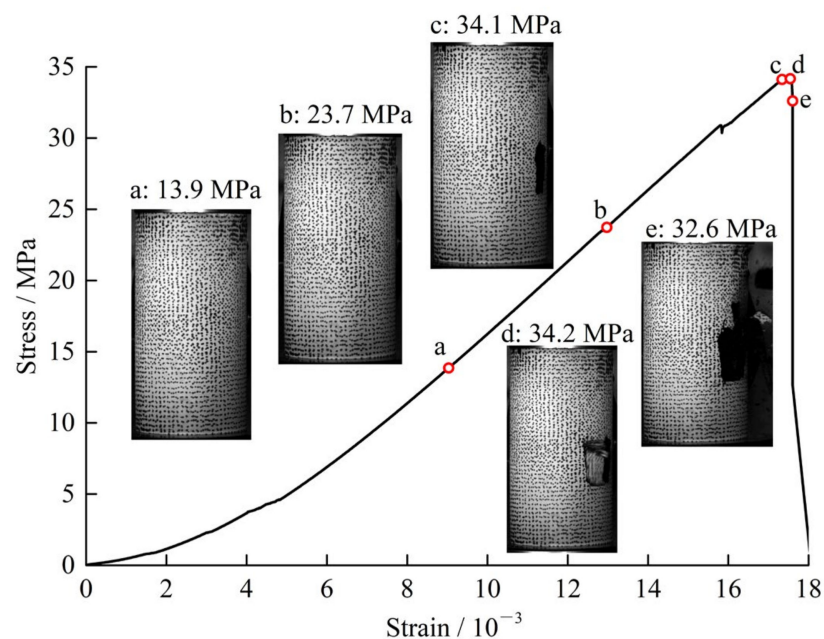


Figure 6. The stress-strain curve and key loading points of specimen H4.

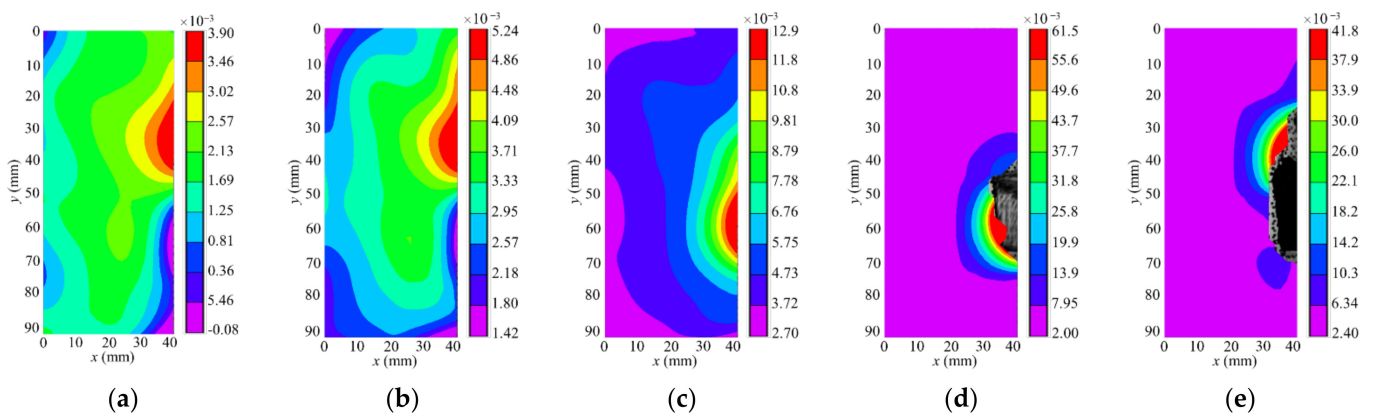


Figure 7. Principal strain fields at different stress stages corresponding to key points (a–e) in Figure 6 (Note compressive strain is taken as negative and tensile strain is taken as positive).

It can be seen from the contours of principal strain, the principal strain gradient is related to the local deformation and local damage. For quantitative description, we arranged a virtual extensometer along the principal strain (the maximum tensile strain) direction on the surface of the specimen to measure the principal strain values in different loading stages. The evolution of the principal strain values in different loading stages (“a”–“e” key points) from the virtual extensometer is shown in Figure 8. During the elastic loading stage (key points “a”–“b”), the principal strain gradient (the slope of the curves in Figure 8b) was not large. When it was loaded to point “c” before the peak point, the principal strain gradient increased significantly in the range of 25 mm–40 mm in the x-axis. Subsequently, local cracks immediately occurred at the peak stress point (key point “d”), where the principal strain reached the maximum. After the peak, the principal strain gradient was significantly reduced, followed by the further expansion of the spalled area until the specimen is completely ruptured.

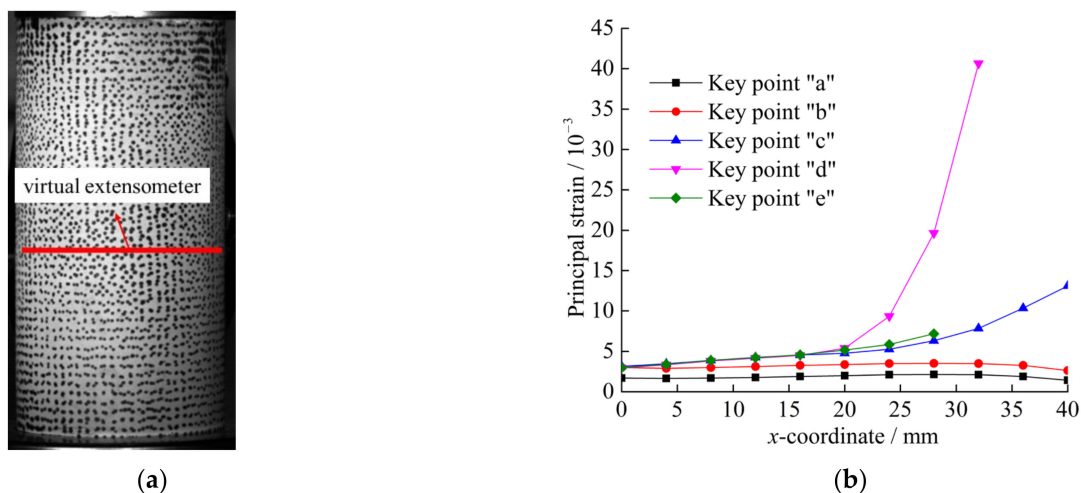


Figure 8. Virtual extensometer layout and principal strain values at different stages: (a) Position of virtual extensometer; (b) Principal strain at different loading stages.

In summary, the local principal strain concentration area is highly consistent with the damaged area of the coal specimen. The expansion of the stress concentration area indicates that the failure of the specimen is imminent, which is well explained by using the principal strain gradient in Figure 8. The area where the principal strain gradient is significantly increased corresponds to the area with the initial fracture, so the principal strain gradient may be a good early warning index for specimen failure.

3.2. Stress-Strain Behaviors and Strength Characteristics

Figure 9 shows the stress-strain curves of coal specimens with both horizontal and vertical bedding at different strain rates. Specifically, the stress-strain curves of the specimens with horizontal bedding are consistent under different strain rates, and can be divided into four stages: compaction, elastic deformation, pre-peak yield, and post-peak failure, as shown in Figure 9a. As the strain rate increases, the compaction stage is shortened, and the corresponding strain is gradually reduced. This is because that the energy received by the specimen per unit time is increased, and the primary fractures are close rapidly. The stress keeps increasing linearly with strain in the elastic stage, and the primary cracks are closed during this stage. The stress acting on the specimen does not create new cracks, and the elastic strain energy is accumulated continuously. The proportion of the elastic deformation stage gradually increases with the increase of strain rate. The plastic yield stage is not apparent at different strain rates, and it occurs in a short time and accounts for a low proportion. At this stage, new cracks are rapidly created and extended. For the post-peak failure stage, the curve is approximately straight downward, showing significant brittleness of the specimens.

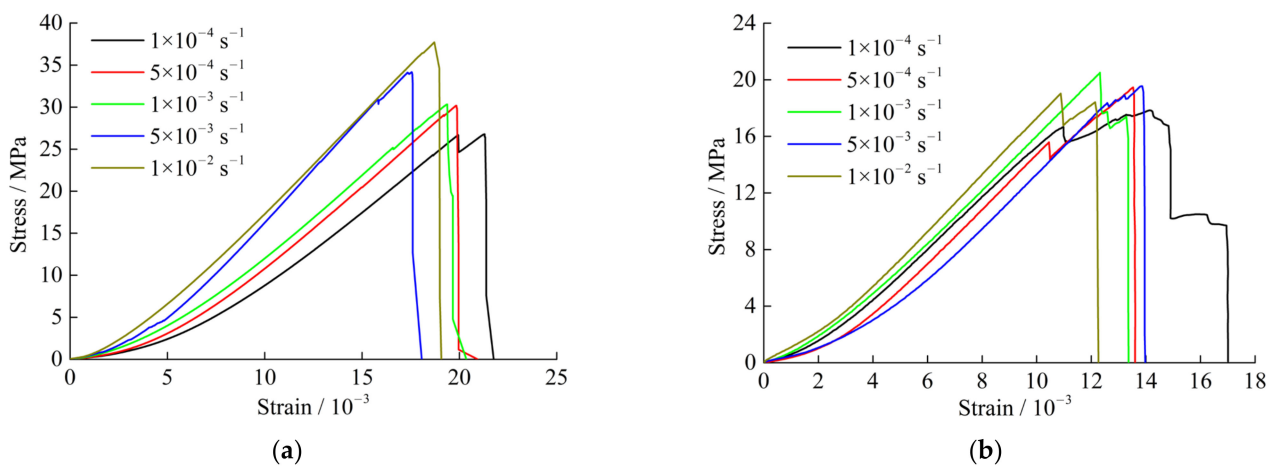


Figure 9. Stress-strain curves under different strain rates: (a) Horizontal bedding; and (b) Vertical bedding.

Figure 9b shows the stress-strain curves of coal specimens with vertical bedding. These specimens also exhibit four stages during loading at different strain rates, but the curve shapes are different, e.g., a longer plastic yield stage ($1 \times 10^{-4} \text{ s}^{-1}$), a corrugated rising yield stage ($5 \times 10^{-3} \text{ s}^{-1}$), and stable deformation prior to the peak.

Figure 10a shows the uniaxial compression strength (UCS) and Figure 10b shows the elastic modulus of coal specimens as a function of strain rate. For specimens with horizontal bedding, as the strain rate is increased from 10^{-5} to 10^{-2} s^{-1} , the UCS of coal specimens is increased from 26.8 MPa to 37.7 MPa, and the elastic modulus is changed from 1.88 GPa to 2.39 GPa, showing significant rate-dependence. The energy theory can explain the strain rate dependency. The initiation and propagation of micro-cracks lead to the damage of coal specimens, and with a large loading rate, the development of micro-cracks lags behind the increment of loading. Because of this “lag”, the energy absorbed by coal specimens cannot be completely consumed or released through the development of micro-cracks in a short time and is temporarily stored in the form of compression, thus leading to the increase in strength. The fitting curve for the UCS appears as a logarithmic function; The variation mode of the UCS with the strain rate may be expressed in Equation (1), and an equation of the relationship between the elastic modulus and the strain rate may be expressed as Equation (2)

$$\sigma = 47.12 + 2.252 \ln \dot{\epsilon} \quad (1)$$

$$E = 3.03 + 0.1293 \ln \dot{\epsilon} \quad (2)$$

where σ is the UCS, E is the elastic modulus and $\dot{\epsilon}$ is strain rate. With the increase of the strain rate, the rate of increment in the UCS is reduced gradually, which is in an agreement with Liu et al. [30], Wang et al. [40], and Lyu et al. [41]. As strain rate increases to a certain degree, the internal fractures of the specimens are not sufficiently closed, resulting in an increase in strength. With the further increase of the strain rate, the damage degree of the specimens will further aggravate with the generation and propagation of new cracks, and the combined rate dependency and the evolution of internal cracks will weaken the growth rate in strength.

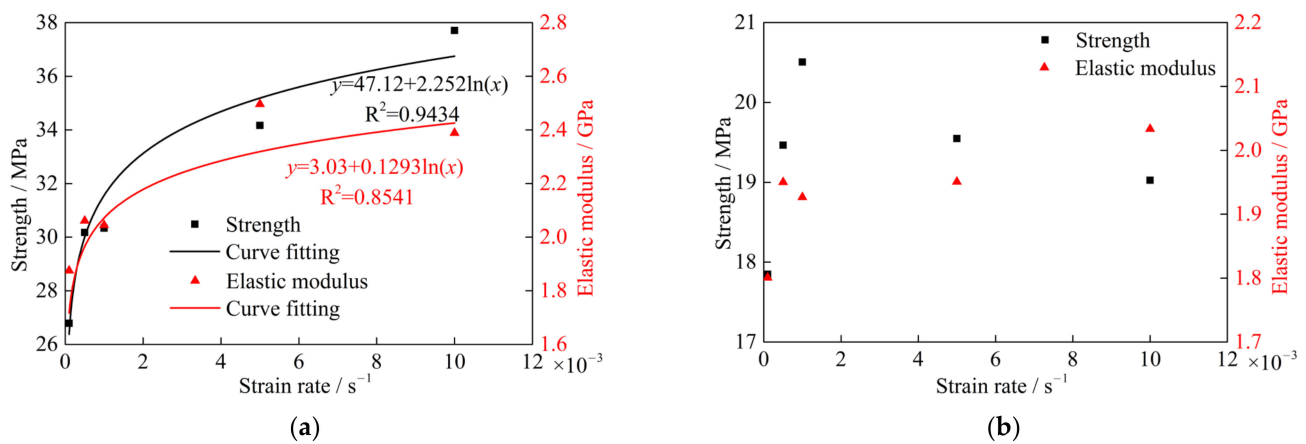


Figure 10. Strength and elastic modulus at different strain rates: (a) Specimens with horizontal bedding; and (b) Specimens with vertical bedding.

The UCS of coal specimens with vertical bedding increases at first and then decreases with increasing strain rate. The strain rate is $1 \times 10^{-3} \text{ s}^{-1}$ when the trend is reversed, at which the maximum strength is 20.5 MPa. Comparing Figure 10a,b, we observe that the coal specimens with vertical bedding have lower strength than that with horizontal bedding at the same strain rate, and the difference further increases with increasing strain rate. The internal cracks in the specimen with vertical bedding are roughly vertical, and tensile stress is created during loading. Because of the low tensile strength in coal, splitting failure occurs easily of the specimens with vertical bedding, as a result, the strength is lower than that of specimens with horizontal bedding. In addition, the internal pre-existing cracks are easier to be reactivated of the specimens with vertical bedding. Cracks extend and penetrate more easily as the strain rate rises to a certain level, therefore, the UCS first increases and then declines.

3.3. Strain Rate and Bedding Effect on AE Characteristics

The AE signals generated in the process of loading are mainly related to the generation, evolution, and coalescence of cracks. When cracks are created and extend, the stored energy is released in the form of waves, and the release of AE energy indicates the generation of damage, and the amplitude of AE signals can characterize the degree of damage. Change of AE energy reflects the crack evolution and coalescence process and the ultimate failure pattern.

Figure 11 shows the strain rate effect on the AE parameters of coal specimens with horizontal bedding. Each scattered point represents a single AE event and its energy; the blue curve represents the cumulative energy evolution, and the red curve represents the entire stress-strain curve. In Figure 11a,b, strain rates are low ranging $1 \times 10^{-4} \text{ s}^{-1}$ to $5 \times 10^{-4} \text{ s}^{-1}$. Many AE signals are recorded, and the cumulative energy of AE increases steadily. In addition, a great quantity of low-energy AE events are generated at the beginning of the loading stage. Coal specimens have sufficient time for the micro-cracks

and defects to close in the compaction stage, thus releasing a large number of AE events. Since there are no new cracks being created, the AE events in the compaction stage are dominated by small energy events (less than 10^2 J). As the applied stress increases, the generation and propagation of new fractures create more AE events with large energy, and the AE events with the largest energy occur at the peak stress. With the increasing strain rate, the number of AE events decreased significantly as shown in Figure 11c,e, and the proportion of low-energy AE events gradually decreases as well. The largest-energy AE events all appear with a magnitude of about 10^5 J at the post-peak stage for different strain rates.

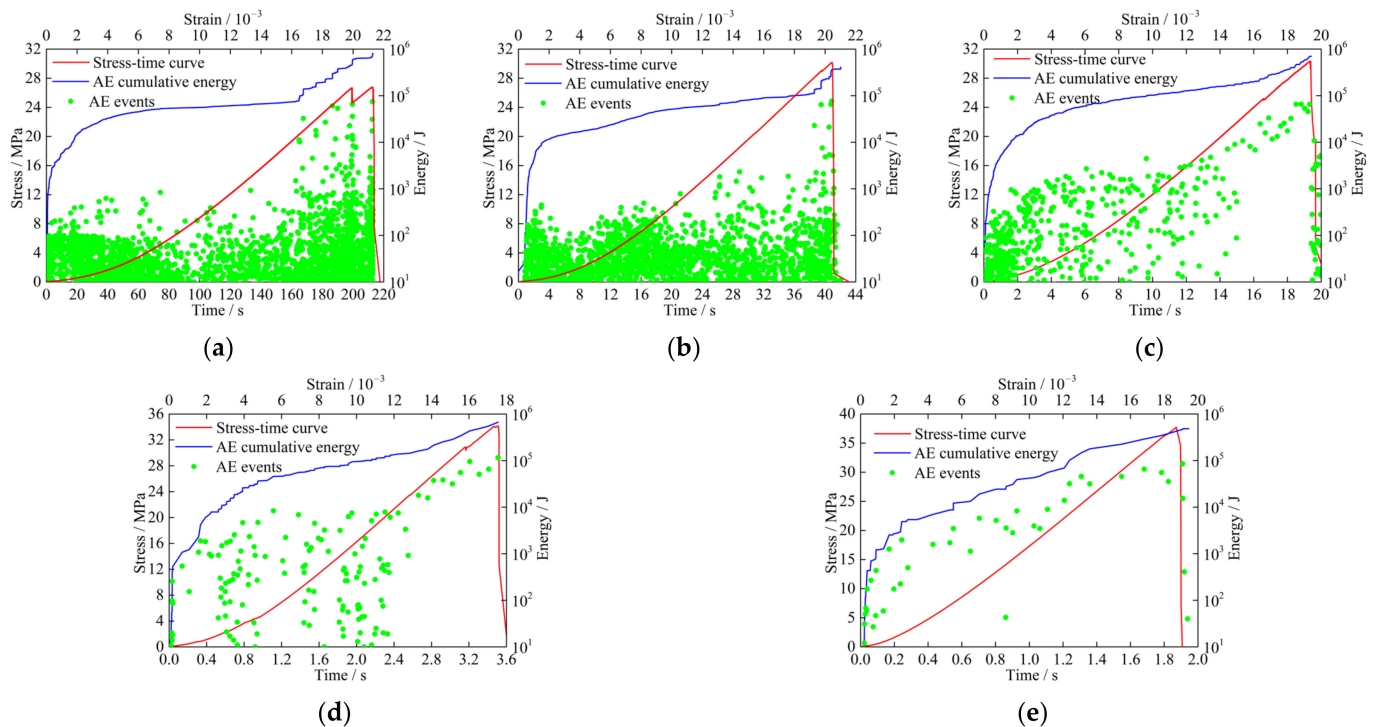


Figure 11. Stress-strain curves and AE characteristics of coal specimens with horizontal bedding: (a) 10^{-4} s^{-1} ; (b) $5 \times 10^{-4} \text{ s}^{-1}$; (c) 10^{-3} s^{-1} ; (d) $5 \times 10^{-3} \text{ s}^{-1}$; (e) 10^{-2} s^{-1} .

Figure 12 shows the strain rate effect on the AE parameters of coal specimens with vertical bedding. AE events are concentrated in the elastic stage and failure stage, and AE events with the largest energy occur after the peak stress, roughly maintaining at about 10^4 J at different strain rates. The cumulative energy curve shows a step-wise increment in the loading process, and the large-energy events are the key factors for the jumps in the curve.

AE characteristics are also closely related to the bedding effect, as illustrated in Figures 11 and 12. When the strain rate is low ($\dot{\epsilon} < 10^{-3} \text{ s}^{-1}$), at the same strain rate, the number of AE events in specimens with horizontal bedding is much larger than that with vertical bedding, and this difference is greatly reduced as the strain rate increases. The percentage of large-energy AE events in coal specimens increases with the strain rate, and the low-energy AE events of specimens with vertical bedding account for the majority at different strain rates. For cumulative AE energy, smooth curves are observed for specimens with horizontal bedding, while stepwise curves with periodic jumps are seen for specimens with vertical bedding. There is a high correlation between AE signal and stress drop, that is, the stress drop point is followed by the occurrence of large-energy AE events. The maximum-energy AE events are only related to the bedding structure and independent of strain rate. Specifically, the maximum energy magnitudes are approximately 10^5 and 10^4 J for specimens with horizontal and vertical bedding, respectively.

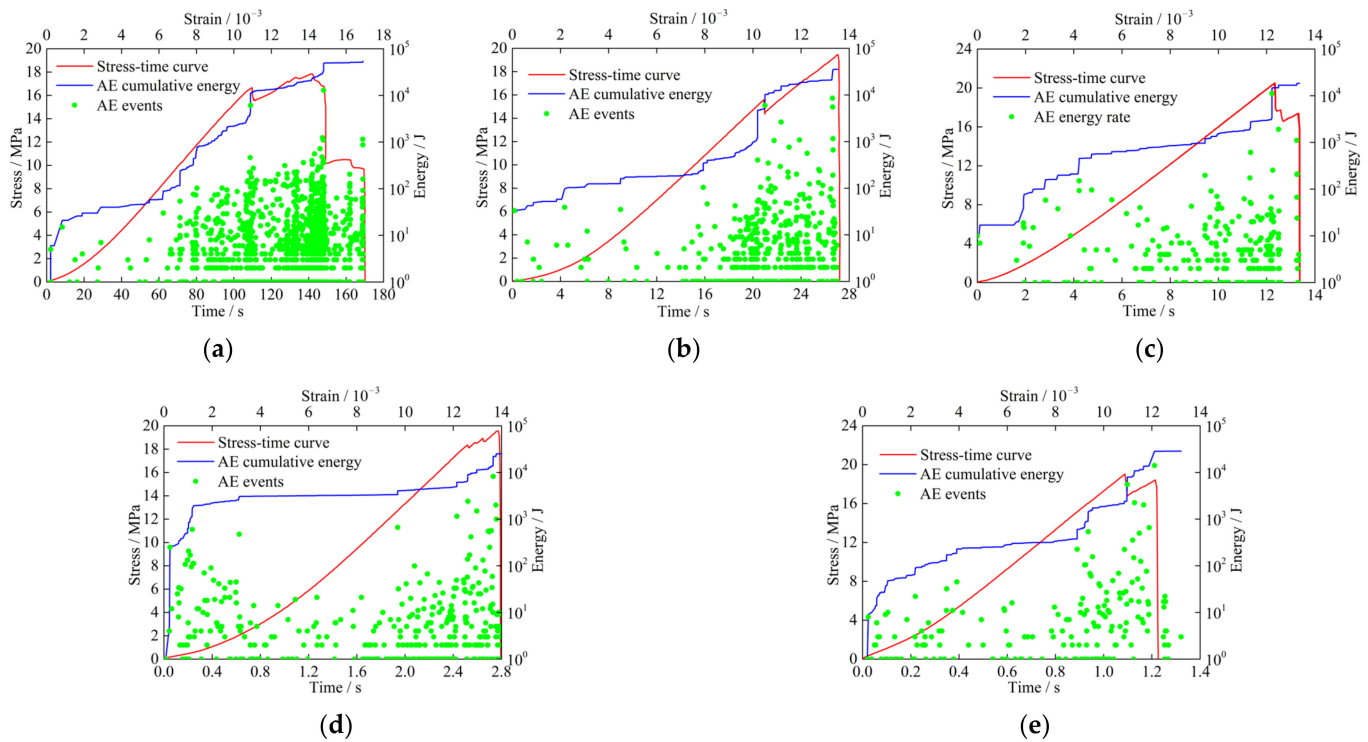


Figure 12. Stress-strain curves and AE characteristics of coal specimens with vertical bedding: (a) 10^{-4} s^{-1} ; (b) $5 \times 10^{-4} \text{ s}^{-1}$; (c) 10^{-3} s^{-1} ; (d) $5 \times 10^{-3} \text{ s}^{-1}$; (e) 10^{-2} s^{-1} .

3.4. Risk Analysis of Rock Burst

To quantitatively analyze AE energy at different strain rates, we define the cumulative energy and energy release rate (energy per unit of time). The cumulative energy is the sum of the AE energy throughout the loading process of a specimen, and the energy release rate is the ratio of the cumulative energy to the loading time. Figure 13 shows the energy evolution of coal specimens at different strain rates. The cumulative energy of the same bedding does not vary with the strain rates, The cumulative energy of coal specimens with horizontal bedding is kept in the range of 10^5 – 10^6 J, and the range is 10^4 – 10^5 J of the specimens with vertical bedding. However, the cumulative energy of the coal specimens with horizontal bedding is much larger than that with vertical bedding. Therefore, the failure mode is burst and ejection failure, the intensity of rupture is much higher. The energy release rate in these specimens increases in the form of a power function with the strain rate, and the relationship between the energy release rate and the strain rate is expressed as,

$$G_1 = 5.85 \times 10^6 \times \dot{\epsilon}^{0.6887} \quad (3)$$

$$G_2 = 5.875 \times \dot{\epsilon}^{1.219} \quad (4)$$

where G_1 and G_2 are the energy release rate with horizontal and vertical bedding at strain rate $\dot{\epsilon}$, respectively. These two equations indicate that the higher the strain rate, the higher the average energy released by micro-cracks during initiation and propagation, which can also lead to more violent failures at higher strain rates. The cumulative energy determines the extent of damage to specimens, and the energy release rate can describe the degree of difficulty of the damage. This means that the ultimate degree of damage to the specimens is basically the same at different strain rates, but the higher the strain rate, the larger the likelihood of damage.

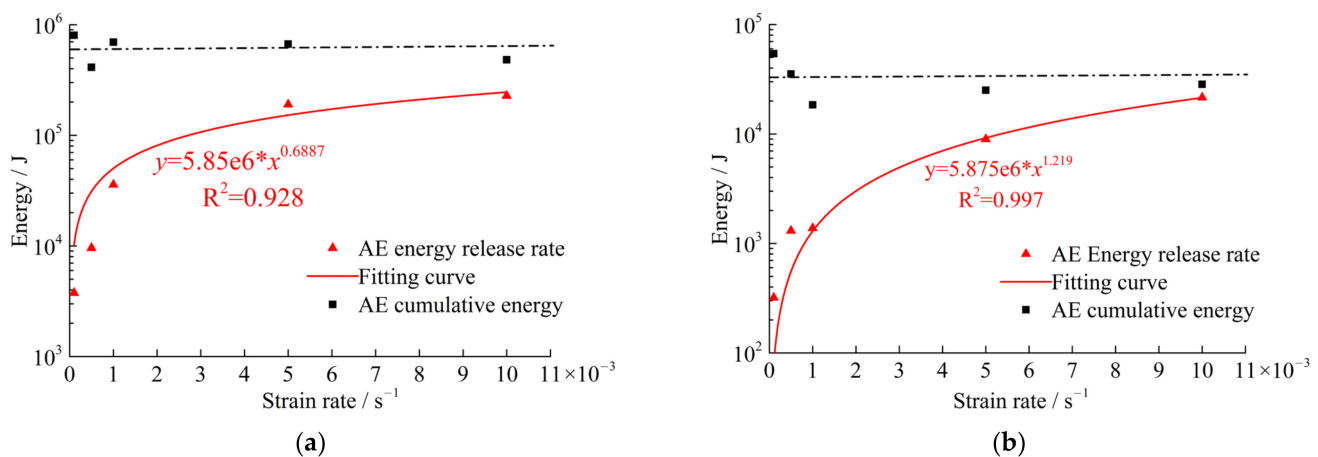


Figure 13. Energy evolution at different strain rates: (a) Horizontal bedding; and (b) Vertical bedding.

We can see from the stress-strain curves (shown in Figure 9), the pre-peak evolution characteristics of these two types of bedded coal specimens are very similar, but the post-peak patterns are different. The stress of the coal specimens with horizontal bedding drops rapidly after the peak, without residual stress. The drop rate is generally faster, clearly indicating brittle failure. Most of the energy stored in the coal specimens is often shown in elastic strain energy, aside from a small amount of energy dissipated before the peak, due to plastic deformation. A great quantity of elastic strain energy is accumulated before the peak, while little strain energy is dissipated permanently by plastic deformation, so the accumulated elastic strain energy is released in the form of kinetic energy. Therefore, a large amount of debris is ejected out when the coal specimen is ruptured, and the risk of rock burst is high.

The post-peak shapes of the stress-strain curves for coal specimens with vertical bedding vary with strain rate, and the post-peak stress declines at a low strain rate of $1 \times 10^{-4} \text{ s}^{-1}$. As the strain rate increases, the time of the yield stage becomes shorter, but there is still a certain residual strength. Due to the propagation of cracks before the peak, a certain amount of energy is consumed, partly due to plastic deformation, so the accumulated elastic strain energy is reduced. In addition, the progressive failure mode delays the failure time and reduces the risk of rock burst.

4. Conclusions

- (1) The failure mode of coal specimens shows a noticeable bedding dependency. The post-peak stress in coal specimens with horizontal bedding decreases rapidly, clearly indicating brittle failure. These specimens generally show an overall burst failure, followed by the ejection of coal fragments in different sizes, with a high risk of rock burst. On the other hand, coal specimens with vertical bedding exhibit a tensile splitting failure, with a low risk of rock burst.
- (2) The UCS of coal specimens is closely related to the bedding direction and the strain rate. With increasing strain rate, the UCS and elastic modulus of specimens with horizontal bedding increases in a logarithmic function. The UCS of coal specimens with vertical bedding increases first, and then decreases as the strain rate keeps increasing, and the strain rate corresponding to the turning point is $1 \times 10^{-3} \text{ s}^{-1}$.
- (3) Strain rate affects the number, distribution, and energy release rate of AE events, but does not change the maximum and cumulative energy of AE events. Specimens with different bedding patterns exhibit differences in the maximum energy and cumulative energy magnitudes and in the cumulative energy curve. The strain rate effect and bedding effect on AE characteristics are essentially related to fracture initiation, propagation, and failure modes.

- (4) A strong correlation exists between the principal strain gradient and the local deformation and local damage. The stage in which the principal strain gradient increases significantly is the fracture initiation stage. The principal strain gradient may be a good early warning index for specimen failure.

Author Contributions: W.C. provided methodology and funding; K.Z. and C.Q. contributed to the experimental operation; K.Z. analyzed the experimental data and wrote the paper; W.Z. and W.C. carefully examined the manuscript and put forward good recommendations before the article was submitted. All authors have read and agreed to the published version of the manuscript.

Funding: This research was funded by the National Natural Science Foundation of China (Grant No. 51991393), the National Natural Science Foundation of China (Grant No. 52079134).

Institutional Review Board Statement: Not applicable.

Informed Consent Statement: Not applicable.

Data Availability Statement: The data that support the findings of this study are available from the corresponding author upon requests.

Acknowledgments: Special thanks for the raw coal samples provided by the Man Jialiang coal mine.

Conflicts of Interest: The authors declare no conflict of interest.

References

1. He, M.C.; Xie, H.P.; Peng, S.P.; Jiang, Y.D. Study on rock mechanics in deep mining engineering. *Chin. J. Rock Mech. Eng.* **2005**, *24*, 2803–2813.
2. Biały, W. Mierzenie właściwości mechanicznych węgla, nowe urządzenia. *J. Geol. Resour. Eng.* **2017**, *1*, 15–23. [[CrossRef](#)]
3. Biały, W. Systemy odmierzające siłę przecięcia węgla—(CCFM). In Proceedings of the 14th SGEM GeoConference on Science and Technologies in Geology, Exploration and Mining, SGEM2014 Conference Proceedings, Albena, Bulgaria, 17–26 June 2014; Volume III, pp. 91–98, ISBN 978-619-7105-09-4/ISSN 1314-2704.
4. Iannacchione, A.T.; Tadolini, S.C. Occurrence, predication, and control of coal burst events in the US. *Int. J. Min. Sci. Technol.* **2016**, *26*, 39–46. [[CrossRef](#)]
5. Hebblewhite, B.; Galvin, J. A review of the geomechanics aspects of a double fatality coal burst at Austar colliery in NSW, Australia in April 2014. *Int. J. Min. Sci. Technol.* **2017**, *27*, 3–7. [[CrossRef](#)]
6. Batugin, A. A proposed classification of the Earth's crustal areas by the level of geodynamic threat. *Geod Geodyn.* **2021**, *12*, 21–30. [[CrossRef](#)]
7. Cao, A.Y.; Jing, G.C.; Ding, Y.L.; Liu, S. Mining-induced static and dynamic loading rate effect on rock damage and acoustic emission characteristic under uniaxial compression. *Saf. Sci.* **2019**, *116*, 86–96. [[CrossRef](#)]
8. Lu, C.P.; Liu, G.J.; Liu, Y.; Zhang, N.; Xue, J.H.; Zhang, L. Microseismic multi-parameter characteristics of rockburst hazard induced by hard roof fall and high stress concentration. *Int. J. Rock Mech. Min. Sci.* **2015**, *76*, 18–32. [[CrossRef](#)]
9. Wang, S.L.; Hao, S.P.; Chen, Y.; Bai, J.B.; Wang, X.Y.; Xu, Y. Numerical investigation of coal pillar failure under simultaneous static and dynamic loading. *Int. J. Rock Mech. Min. Sci.* **2016**, *84*, 59–68. [[CrossRef](#)]
10. McGarr, A. Energy budgets of mining-induced earthquakes and their interactions with nearby stopes. *Int. J. Rock Mech. Min. Sci.* **2000**, *37*, 437–443. [[CrossRef](#)]
11. Mansurov, V.A. Prediction of rockbursts by analysis of induced seismicity data. *Int. J. Rock Mech. Min. Sci.* **2001**, *38*, 893–901. [[CrossRef](#)]
12. He, J.; Dou, L.M.; Cai, W.; Li, Z.L.; Ding, Y.L. In situ test study of characteristics of coal mining dynamic load. *Shock. Vib.* **2015**, *2015*, 121053. [[CrossRef](#)]
13. Roberts, M.; Brummer, R. Support requirements in rockburst conditions. *J. South. Afr. Inst. Min. Metall.* **1988**, *88*, 97–104.
14. Kaiser, P.K.; Tannant, D.D.; McCreath, D.R. *Canadian Rockburst Support Handbook*; Geomech Research Centre, Laurentian University: Sudbury, ON, Canada, 1996.
15. Zhang, Z.X.; Kou, S.Q.; Jiang, L.G.; Lindqvist, P.A. Effects of loading rate on rock fracture: Fracture characteristics and energy partitioning. *Int. J. Rock Mech. Min. Sci.* **2000**, *37*, 745–762. [[CrossRef](#)]
16. Field, J.E.; Walley, S.M.; Proud, W.G.; Goldrein, H.T.; Siviour, C.R. Review of experimental techniques for high rate deformation and shock studies. *Int. J. Impact. Eng.* **2004**, *30*, 725–775. [[CrossRef](#)]
17. Zhang, Q.B.; Zhao, J. A review of dynamic experimental techniques and mechanical behaviour of rock materials. *Rock Mech. Rock Eng.* **2014**, *47*, 1411–1478. [[CrossRef](#)]
18. Tarasov, B.G. Simplified method for determining the extent to which strain rate affects the strength and energy capacity of rock fracture. *J. Min. Sci.* **1990**, *26*, 315–320. [[CrossRef](#)]

19. Zhao, J.; Li, H.B.; Wu, M.B.; Li, T.J. Dynamic uniaxial compression tests on a granite. *Int. J. Rock Mech. Min. Sci.* **1999**, *36*, 273–277. [[CrossRef](#)]
20. Cai, M.; Kaiser, P.K.; Suorineni, F.; Su, K. A study on the dynamic behavior of the Meuse/Hhaute-Marne argillite. *Phys. Chem. Earth* **2007**, *32*, 907–916. [[CrossRef](#)]
21. Wang, Y.; Li, X.; Zheng, B. Stress-strain behavior of soil-rock mixture at medium strain rates-response to seismic dynamic loading. *Soil. Dyn. Earthq. Eng.* **2017**, *93*, 7–17. [[CrossRef](#)]
22. Tan, L.H.; Ren, T.; Yang, X.H.; He, X.Q. A numerical simulation study on mechanical behaviour of coal with bedding planes under coupled static and dynamic load. *Int. J. Min. Sci. Technol.* **2018**, *28*, 791–797. [[CrossRef](#)]
23. Feng, J.J.; Wang, E.Y.; Chen, X.; Ding, H.C. Energy dissipation rate: An indicator of coal deformation and failure under static and dynamic compressive loads. *Int. J. Min. Sci. Technol.* **2018**, *28*, 397–406. [[CrossRef](#)]
24. Wang, W.; Wang, H.; Li, D.; Li, H.; Liu, Z. Strength and failure characteristics of natural and water-saturated coal specimens under static and dynamic loads. *Shock. Vib.* **2018**, *2018*, 3526121. [[CrossRef](#)]
25. Li, M.; Liang, W.; Yue, G.; Zheng, X.; Liu, H. Dynamic mechanical properties of structural anisotropic coal under low and medium strain rates. *PLoS ONE* **2020**, *15*, e0236802. [[CrossRef](#)]
26. Huang, B.X.; Liu, J.G. The effect of loading rate on the behavior of samples composed of coal and rock. *Int. J. Rock Mech. Min. Sci.* **2013**, *61*, 23–30. [[CrossRef](#)]
27. Bragova, A.M.; Lomunova, A.K.; Sergeicheva, I.V.; Tsembelisb, K.; Proud, W.G. Determination of physicommechanical properties of soft soils from medium to high strain rates. *Int. J. Impact. Eng.* **2008**, *35*, 967–976. [[CrossRef](#)]
28. Zhao, Y.X.; Liu, S.M.; Zhao, G.F.; Elsworth, D.; Jiang, Y.D.; Han, J.L. Failure mechanisms in coal: Dependence on strain rate and microstructure. *J. Geophys. Res. Solid Earth* **2014**, *119*, 6924–6935. [[CrossRef](#)]
29. Liang, C.Y.; Wu, S.R.; Li, X.; Xin, P. Effects of strain rate on fracture characteristics and mesoscopic failure mechanisms of granite. *Int. J. Rock Mech. Min. Sci.* **2015**, *76*, 146–154. [[CrossRef](#)]
30. Liu, X.L.; Liu, Z.; Li, X.B.; Gong, F.Q.; Du, K. Experimental study on the effect of strain rate on rock acoustic emission characteristics. *Int. J. Rock Mech. Min. Sci.* **2020**, *133*, 104420. [[CrossRef](#)]
31. Li, S.G.; Du, X.H.; Zhao, P.X.; Xiao, P.; Lin, H.F.; Shuang, H.Q. Experimental study on crack evolution characteristics of rock-like materials under different strain rates. *J. Geophys. Eng.* **2018**, *15*, 2071–2078.
32. Li, D.Y.; Gao, F.H.; Han, Z.Y.; Zhu, Q.Q. Experimental evaluation on rock failure mechanism with combined flaws in a connected geometry under coupled static-dynamic loads. *Soil. Dyn. Earthq. Eng.* **2020**, *132*, 106800. [[CrossRef](#)]
33. Song, H.; Zhang, H.; Fu, D.; Kang, Y.; Huang, G.Y.; Qu, C.Y.; Cai, Z.X. Experimental study on damage evolution of rock under uniform and concentrated loading conditions using digital image correlation. *Fatigue Fract. Eng. Mater. Struct.* **2013**, *36*, 760–768. [[CrossRef](#)]
34. Dong, W.; Wu, Z.M.; Zhou, X.M.; Wang, N.; Kastiukas, G. An experimental study on crack propagation at rock-concrete interface using digital image correlation technique. *Eng. Fract. Mech.* **2017**, *171*, 50–63. [[CrossRef](#)]
35. Wasantha, P.L.P.; Ranjith, P.G.; Shao, S.S. Energy monitoring and analysis during deformation of bedded-sandstone: Use of acoustic emission. *Ultrasonics* **2014**, *54*, 217–226. [[CrossRef](#)] [[PubMed](#)]
36. Tavallali, A.; Vervoort, A. Failure of layered sandstone under Brazilian test conditions: Effect of micro-scale parameters on macro-scale behaviour. *Rock Mech. Rock Eng.* **2010**, *43*, 641–653. [[CrossRef](#)]
37. Rongkun, P.; Dong, F.; Minggao, Y.; Lei, C. Directivity effect of unloading bedding coal induced fracture evolution and its application. *Int. J. Min. Sci. Technol.* **2017**, *27*, 825–829. [[CrossRef](#)]
38. Liu, X.H.; Dai, F.; Zhang, R.; Liu, J.F. Static and dynamic uniaxial compression tests on coal rock considering the bedding directivity. *Environ. Earth. Sci.* **2015**, *73*, 5933–5949. [[CrossRef](#)]
39. Lu, Z.G.; Ju, W.J.; Wang, H.; Zheng, J.W.; Yi, K.; Feng, Y.L.; Sun, L.W. Experimental study on anisotropic characteristics of impact tendency and failure model of hard coal. *Chin. J. Rock Mech. Eng.* **2019**, *38*, 757–768.
40. Wang, Q.S.; Chen, J.X.; Guo, J.Q.; Luo, Y.B.; Li, Y.; Wang, H.Y.; Liu, Q. Strain Rate Effect on Acoustic Emission Characteristics and Energy Mechanisms of Karst Limestone under Uniaxial Compression. *Adv. Materi. Sci. Eng.* **2020**, *1*, 1–13. [[CrossRef](#)]
41. Lyu, P.; Chen, X.H.; Chen, G.B.; Qiu, L. Experimental study on dynamic mechanical responses of coal specimens under the combined dynamic-static loading. *Arab. J. Geosci.* **2020**, *13*, 935. [[CrossRef](#)]